ACS APPLIED MATERIALS & INTERFACES

Research Article

www.acsami.org

Which Oxide for Low-Emissivity Glasses? First-Principles Modeling of Silver Adhesion

David Cornil,*[,†] Hugues Wiame,[‡] Benoit Lecomte,[‡] Jérôme Cornil,[†] and David Beljonne[†]

[†]Laboratory for Chemistry of Novel Materials, University of Mons (UMONS), Place du Parc 20, 7000 Mons, Belgium

[‡]AGC Glass Europe Technovation Centre, rue Louis Blériot 12, 6041 Gosselies, Belgium

Supporting Information

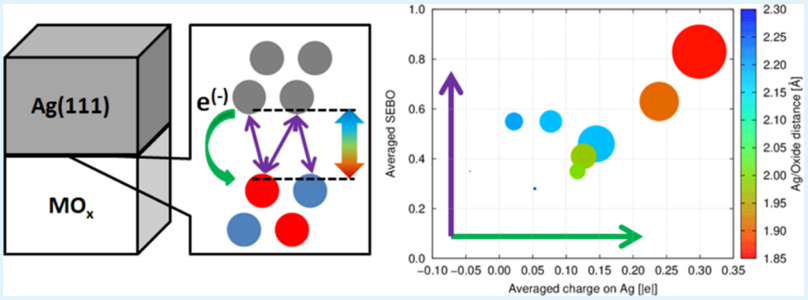

ABSTRACT: Density functional theory (DFT) calculations were performed to assess the work of adhesion of silver layers deposited on metal oxide surfaces differing by their chemical nature (ZnO, TiO_2, SnO_2, and ZrO_2) and their crystallographic face. The calculated work of adhesion values range from ~0 to 3 J m^{-2} and are shown to originate from the interplay between ionic (associated with charge transfer at the interface) and covalent (as probed by atomic bond orders between silver and the metal oxide atoms) interactions. The results are discussed in the context of the design of silver/metal oxide interfaces for low-emissivity glasses.

KEYWORDS: *work of adhesion, interface, metal oxide, silver, DFT*

1. INTRODUCTION

Nowadays, low-emissivity (or low-e) glasses are ubiquitous in everyday life, e.g. they are used in buildings and cars.[1,2] The functionalities of these glasses are related to their particular architecture based on a thin metal layer sandwiched between oxide thin films. Depositing silver layers on window glasses indeed lowers the emission of radiant thermal energy. During the last decades, various and complex stacking structures have been investigated to achieve low-e properties with the most typical structures combining silver as a metal and transparent oxide layers such as ZnO, SnO_2, TiO_2, etc.[3−10]

Interfaces play a key role in such heterostructures and should, obviously, promote a strong adhesion between the two layers.[11] A high affinity between the two surfaces is indeed expected to reduce the number of weak points (fracture modes) and to ensure low mechanical stress at the interface, resistance to degradation, etc.[12−18] A convenient observable to quantify the adhesion between two solids is the work of adhesion, W_{12}, namely, the work required to bring the surfaces from close contact to infinite distance. The development of low-e glasses has thus motivated theoretical investigations of a number of metal/metal oxide interfaces.[19−26] Yet, detailed mechanistic studies relating the work of adhesion to interfacial electronic processes and how it can be tuned by proper surface engineering are lacking.

Here, we report density functional theory (DFT) calculations of the work of adhesion of silver with metal oxides varying in chemical composition (ZnO, SnO_2, TiO_2, and ZrO_2) and by their contact crystallographic face. We show that W_{12} results from the interplay between charge transfer ("ionic") and wave function overlap ("covalent") contributions at the hetero-junction.

2. METHODOLOGY

2.1. Construction of the Interfaces. The interface models were built as follows. First, we generated separately five-layer slabs of silver and metal oxide on the basis of experimental X-ray data for the corresponding materials. The size of the silver and metal oxide supercells was chosen to maximize size commensurability at the interface; see the section below. The geometry of the metal oxide surfaces was allowed to fully relax prior the deposition of silver. The silver layer was then brought in contact with the metal oxide surface, and the full interface geometry was fully optimized. These geometries were subsequently used to compute the electronic properties (charges and bond-orders) in the stacked structures. The models and optimized geometries used for the various

Received: March 7, 2017
Accepted: May 9, 2017
Published: May 9, 2017

DOI: 10.1021/acsami.7b03269
ACS Appl. Mater. Interfaces 2017, 9, 18346−18354

interfaces are shown in Figure 1 (see also (A) in Figures S1−9 for a top view of the contact planes for each interface).

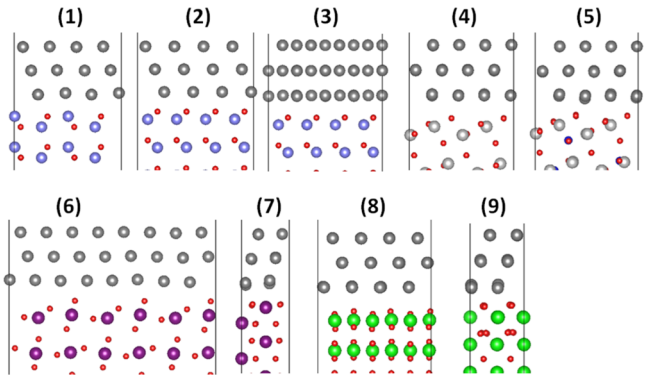

Figure 1. Side view of all silver/metal oxide models investigated in this study around the interface region. Each interface involves a five-layer Ag(111) surface in contact with ZnO($10\bar{1}0$) (1), ZnO($000\bar{1}$) with low density of silver (2), ZnO($000\bar{1}$) with high density of silver (3), anatase TiO_2(101) (4), nitrogen-doped anatase TiO_2(101) (5), SnO_2(110) (6), SnO_2(100) (7), ZrO_2(111) (8), and ZrO_2 (100) (9).

2.1.1. Silver Slab. Silver bulk displays a face centered cubic lattice ($Fm\bar{3}m$) with cell parameters a = 4.08 Å. From the bulk, we generated a 5-layer slab with a terminated (111) surface. This face is selected as it is the silver surface with the lowest surface energy and hence generally observed experimentally.[27] Moreover, our calculations show that an atom-by-atom deposition of silver onto the metal oxide surface spontaneously leads to the formation of the (111) facet. The (111) surface consists of silver atoms arranged in a hexagonal pattern with an Ag−Ag bond length of ca. 2.90 Å and adjacent silver layers arranged following an A−B−C packing. This surface was put in contact on top of the different metal oxide layers. The lattice vectors of the unit cell used for the interface model have been arbitrary chosen from the lattice vectors of the metal oxide unit, hence inducing a small compressive or tensile stress in the silver layers to match the size of the metal oxide surface (see Section 2.2).

2.1.2. Metal Oxide Slabs. Similarly to the silver surface, the metal oxide slabs were generated from the corresponding experimental bulk structure. We focused in this work on surfaces generated from four different oxides typically used in the glass industry: zinc oxide (ZnO), titanium dioxide (TiO_2), tin-dioxide (SnO_2), and zirconium dioxide (ZrO_2).

ZnO. For ZnO, we considered the bulk wurzite with parameters a = 3.25 Å and c = 5.21 Å, from which we generated the ($10\bar{1}0$) and ($000\bar{1}$) faces. The ($10\bar{1}0$) surface consists of a stoichiometric amount of oxygen and zinc atoms at the top of the surface. For this reason, this face is generally referred as the nonpolar surface and is the most commonly used at the theoretical level for fundamental and benchmarking studies.[28] However, the ($000\bar{1}$) direction is observed to be the preferential one for the ZnO growth.[29] In this case, the slab is terminated by an oxygen-rich surface on one side and a zinc-rich surface on the opposite side and is hence referred to as the polar surface. Here, we considered only the terminated oxygen face in contact with the silver layers as it yields a much stronger adhesion.[24,30]

TiO_2. The anatase form of titanium dioxide was adopted. This allotropic form has a tetragonal symmetry with cell parameters a = 3.78 Å and c = 9.51 Å. From this unit cell, we generated the (110) face, which is the most stable according to both experimental investigations and DFT predictions.[31,32] To investigate the impact of doping, we also considered the (110) surface in which some oxygen atoms were arbitrary substituted by nitrogen atoms to generate a p-doped surface at a doping ratio close to 5%.

SnO_2. SnO_2 condenses in the rutile structure with the bulk parameters a = 4.74 Å and c = 3.19 Å. From the bulk, we prepared the (100) and (110) surfaces, i.e., the natural growing faces of SnO_2.[33] The (110) surface is thermodynamically the most stable among the two.[34−36] Different surface reconstruction processes have been suggested for this face.[37,38] Here, we considered for (110) only a bulk terminated face with bridging oxygen atoms at the top. The (100) face is nonpolar with tin and oxygen atoms present on the surface in a stoichiometric ratio.

ZrO_2. Zirconia has also been studied in the context of metal adhesion, namely transition metals such as Ni, Pt, or Pd adsorbed on various ZrO_2 surfaces have been previously modeled.[19,20] Zirconia in its cubic form has parameter a = 5.17 Å. In a similar way as for ZnO, we selected polar and nonpolar surfaces. The nonpolar is the (111) plane, also energetically the most stable,[19,39−41] while the polar is the (100) plane, exhibiting a terminated oxygen-rich surface.[40,42]

2.2. Commensurability. The main issue when building models for interfaces between two solids is commensurability. The structural disparity between two surfaces in contact can be described by a misfit quantity M defined as[43−45]

$$M = 1 - \frac{2\Omega}{A_1 + A_2} \quad (1)$$

where A_1 and A_2 are the area of the two surfaces in contact and Ω is the overlap area. One can also calculate along the two directions of the surface the lattice mismatch strain:[46]

$$f = \frac{l_s - l_e}{l_e} \quad (2)$$

where l_s is the lattice vector of the substrate (the metal oxide in this case) and l_e is the lattice vector of the epitaxial layer (i.e., the silver layers) deposited on the substrate. In contrast to the misfit value that is always positive, the mismatch strain can either be positive or negative corresponding to tensile ($f > 0$) or compressive ($f < 0$) behavior of the epitaxial layer.

Two approaches can be used to ensure commensurability between two surfaces. The first one is the (1 × 1) approximation model, where the interface is generated by contact of the primitive cell of the two solids. This method is largely used for interface studies at the first-principles level but is limited to solids whose lattice constants differ by a few percents only.[30,47−50] However, it has been shown in the context of adhesion study that accurate work of separation can still be obtained with an optimized (1 × 1) model, even for a large mismatch (>30%) between the primitive cells.[51] The other approach consists in generating a semicoherent interface (i.e., an interface where there is a partial lattice matching between the two phases) by construction of an (a × b) supercell whose a and b lattice vectors are multiples of the primitive lattice parameters of the two solids (see Figure 2).[24,52−55] We selected this second approach because large mismatches can be observed for some structures. For example, in the case of the ZrO_2(111)/Ag(111) interface, the lattice vectors of the primitive cells are (5.07 × 5.07 Å) for ZrO_2 and

DOI: 10.1021/acsami.7b03269
ACS Appl. Mater. Interfaces 2017, 9, 18346−18354

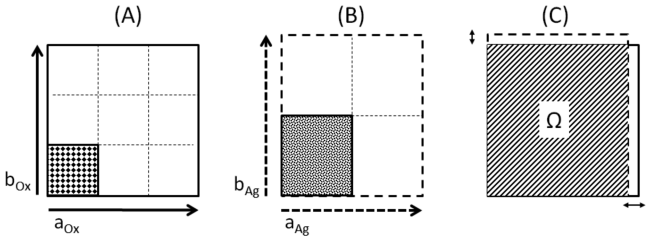

Figure 2. Scheme of the methodology applied to build the interface model and to calculate the commensurability between the silver and metal oxide surface. (A) A supercell is generated to model the metal oxide surface by repetition along the *a*- and *b*-axes of the experimental unit cell (filled square). (B) A similar procedure is applied for the silver surface. In this example, $a_{Ag} < a_{Ox}$ and $b_{Ag} > b_{Ox}$. (C) The silver and metal oxide slabs are brought in contact to generate the interface. The size of the supercell in panels A and B was chosen to maximize the overlap area between the two supercells, Ω.

(2.91 × 5.04 Å) for silver. This represents a ratio between the lattice parameters of 0.57 (approximately 3/5) along the *a*-axis and 0.99 along the *b*-axis. Thus, an interface model of (3 × 1)ZrO_2/(5 × 1)Ag was generated with supercell parameters of (15.21 × 5.07 Å). This leads to a mismatch of 4.5% along the *a*-direction to be compared with 74.2% in the (1 × 1) model.

The misfit parameter and lattice mismatch calculated for all generated interface models are compiled in Table 1. The misfit parameter is found to be below 10% in all cases except for the polar ZnO surface (entry 2 in Table 1). For this particular case, the most stable adsorption sites for silver atoms correspond to bridge-hollow positions where silver atoms occupy the center of the triangle patterns defined by the oxygen atoms at the surface (see Supporting Information, Figure S2A). This creates upon relaxation an adsorbed layer of silver with a density that is lower by 25% compared to the (111) surface obtained from bulk silver. To prepare an Ag/ZnO(000$\bar{1}$) interface with a silver density approaching the bulk value, we used a silver slab with 16 silver atoms on the surface (instead of 12 in entry 2) to build the interface listed as entry 3 in Table 1. There, the silver layer undergoes a compressive stress to match the lattice parameters of the oxide.

2.3. Computational Details. Our calculations were performed at the DFT level with periodic boundary conditions as implemented in the SIESTA code.[56] The exchange-correlation functional was described in the Generalized Gradient Approximation using the PBE functional.[57] A numerical atomic basis set was adopted for the valence electrons using a real-space grid with a mesh-cutoff of 400 Ry, while core electrons are described by Troullier−Martin pseudopotentials.[58] A Monkhorst−Pack grid was used for the generation of the k-space.[59] The dimension of the grid was adapted for each silver/metal oxide interface depending on the size of the supercell to generate similarly resolved k-space (see Table 1). First, the atomic positions in the metal oxide slabs, generated from the corresponding bulk geometry, were allowed to fully relax. The geometric relaxation was performed using the conjugated-gradient formalism with a convergence criteria on the atomic forces of 0.04 eV $Å^{-1}$. The lattice vectors of the slab unit cell were kept fixed to their bulk values during this first relaxation protocol. The silver slab was prepared using the same approach and then deposited on the oxide surface, using as the initial silver/oxide interface distance a value of 2.0 Å. The structure of the complete interface (oxide plus silver) was then allowed to fully relax. The net atomic charges and atomic bond orders were computed for the fully relaxed structures from the electronic density generated by SIESTA using the DDEC6 charge density partition scheme developed by Manz et al.[60,61]

3. RESULTS AND DISCUSSION

The work of adhesion, W_{12}, measures the affinity of the silver for the oxide surfaces. W_{12} can be defined using the difference in the total energy between the interface and the two isolated surfaces, normalized per surface area:[50,55,62,63]

$$W_{12} = \frac{[E_{Ag} + E_{Ox}] - E_{Ag/Ox}}{A} \quad (3)$$

where E_{Ag}, E_{Ox}, and $E_{Ag/Ox}$ are the total energies computed within the interfacial geometry for the silver layers, oxide layers, and full interfaces, respectively, and A is the area of the interface.

The interfaces considered in this study yield work separation values spanning a large range from ∼0 J m^{-2} (no affinity of the silver for the oxide) up to ca. 3 J m^{-2} (strong interaction between the two surfaces) (Table 2). Zinc oxide surfaces demonstrate a high affinity with the silver layers with W_{12} of 0.959, 2.086, and 1.956 J m^{-2} for the interfaces involving ZnO(10$\bar{1}$0), ZnO(000$\bar{1}$) (12), and ZnO(000$\bar{1}$) (16), respectively; thus, the polar surfaces yield a stronger adhesion. The higher affinity for the polar versus the nonpolar surfaces can be explained by the Zn/O stoichiometry at the surface and its impact on the interfacial charge transfer, as described below.

These values are consistent with the interfacial toughness at the ZnO//Ag and Ag//ZnO interfaces, measured between 1.0 and 2.8 J m^{-2} depending on the nature of the sublayers or the growth mechanism.[3] Unfortunately, such data are lacking for many oxides considered here. We hope that our work will motivate further experimental investigations to verify our

Table 1. Misfit Value (M) and Lattice Mismatch Strain (f) for the Interface Models Investigated[a]

interface	M (%)	f_a (%)	f_b (%)	$(a \times b)$ (Å^2)	$k_a \times k_b \times k_c$
(1) ZnO(10$\bar{1}$0)‖Ag(111)	7.0	3.2	11.6	10.40 × 9.75	(5 5 1)
(2) ZnO(000$\bar{1}$)‖Ag(111) (12)	11.0	11.7	11.7	9.75 × 12.26	(5 4 1)
(3) ZnO(000$\bar{1}$)‖Ag(111) (16)	3.3	−3.3	−3.3	9.75 × 12.26	(5 4 1)
(4) TiO_2(101)‖Ag(111)	2.0	−2.7	1.2	11.33 × 10.21	(4 5 1)
(5) TiO_2:N(101)‖Ag(111)	2.0	−2.7	1.2	11.33 × 10.21	(4 5 1)
(6) SnO_2(110)‖Ag(111)	4.7	9.6	−0.3	3.19 × 20.10	(15 2 1)
(7) SnO_2(100)‖Ag(111)	6.9	8.5	−6.0	9.47 × 4.74	(5 10 1)
(8) ZrO_2(111)‖Ag(111)	6.5	6.7	6.7	10.76 × 12.42	(5 4 1)
(9) ZrO_2(100)‖Ag(111)	2.5	4.5	0.6	15.21 × 5.07	(3 10 1)

[a] a and b are the lattice vectors of the supercells, and k is the number of k-points used in each direction for the sampling of the Brillouin zone.

DOI: 10.1021/acsami.7b03269
ACS Appl. Mater. Interfaces 2017, 9, 18346−18354

Table 2. Interfacial Properties of the Investigated Structures[a]

interface	N_{Ag}	d_{Ag-Ox} (Å)	q_{Ag} (|e|)	SEBO	W_{12} (J m^{-2})
ZnO(10$\bar{1}$0)‖Ag(111) (1)	12	2.20	0.022	0.55	0.959
ZnO(000$\bar{1}$)‖Ag(111) (12) (2)	12	1.91	0.239	0.63	2.086
ZnO(000$\bar{1}$)‖Ag(111) (16) (3)	16	2.18	0.145	0.46	1.956
TiO_2(101)‖Ag(111) (4)	16	2.26	0.053	0.28	0.159
TiO_2:N(101)‖Ag(111) (5)	16	1.98	0.126	0.41	1.364
SnO_2(110)‖Ag(111) (6)	8	2.00	0.117	0.35	0.862
SnO_2(100)‖Ag(111) (7)	6	2.18	0.077	0.55	1.201
ZrO_2(111)‖Ag(111) (8)	16	2.30	−0.044	0.35	0.060
ZrO_2(100)‖Ag(111) (9)	10	1.86	0.299	0.83	2.876

[a] N_{Ag} is the number of silver atoms per layer; d_{Ag-Ox} the distance between the metal oxide and the silver layers (average difference between the position of the silver atoms in the first layer and the top atoms of the metal oxide), and q_{Ag} is the averaged charge per silver atom in the first silver layer. SEBO and W_{12} are the sum of the effective bond orders for silver and the work separation, respectively.

theoretical predictions. Theoretical investigations on the Ag(111)/ZnO(000$\bar{1}$) have reported values going to 0.7 up to more than 4.0 J m^{-2} depending on the interface model and the lattice mismatch or the relative position of the two surfaces.[24,30,64]

With respect to ZnO, TiO_2 shows very poor adhesion with W_{12} = 0.159 J m^{-2}. Similar weak adhesions for the TiO_2/Ag(111) interface were obtained theoretically using rutile and anatase surfaces with value of ca. 0.2 J m^{-2} (on anatase) and 0.4 J m^{-2} (on rutile).[53] Very interestingly, p-type doping was found to grandly improve the adhesion with a 1 order of magnitude increase in W_{12} for 5% doped N:TiO_2 (W_{sep} = 1.364 J m^{-2}). This is consistent with modeling work pointing to the improvement in adhesion using an under-stoichiometric TiO_{2-x} surface.[53]

The two SnO_2 planes have an affinity for silver comparable to that of the nonpolar ZnO with W_{12} values of 0.9 and 1.2 J m^{-2} computed for the (110) and (100) surface planes, respectively. These values are consistent with other reported data using first-principles calculations.[38] Finally, the adhesion between silver and ZrO_2 surfaces cranks up from 0.06 to 2.88 J m^{-2} when going from the (111) to the (100) surface, underlining the role of the crystal face on adhesion. In order to rationalize these data, we investigated the electronic properties at the interface between the two layers. The magnitude of the work of adhesion is driven by the overlap between wave functions of the two components yielding hybridized interfacial states and a partial or full charge transfer taking place to equilibrate the chemical potential of the two contacted slabs and drive the system to equilibrium. We refer below to these two contributions as covalent (or mixed) and ionic, respectively. We first sought for a correlation between the work of separation and the direction and amount of charge transfer between the silver layer and the oxide surface. The charge reorganization at the interface was analyzed through the profile of the charge density difference, $\Delta\rho$, using a macroscopic average technique.[65]

$$\Delta\rho = \rho_{int} - (\rho_{Ag} + \rho_{M-Ox}) \quad (4)$$

where ρ_{int}, ρ_{Ag}, and ρ_{M-Ox} are the charge density of the full interface, the silver layers, and the metal oxide layers, respectively.

The atomic charges were computed here using the DDEC6 partition scheme. Because the charge density profile shows modifications localized within the silver plane in direct contact with the metal oxide, we considered only the silver atoms belonging to the interfacial layer in our analysis (while normalizing the net charge of the layer by the number of silver atoms to ease comparison between the different interface models). The resulting average charges per silver atom at the contact layer, q_{Ag}, are collected in Table 2. A positive value was obtained for all models (expect for interface 8), thus pointing to a ground-state electron transfer from the silver layer to the

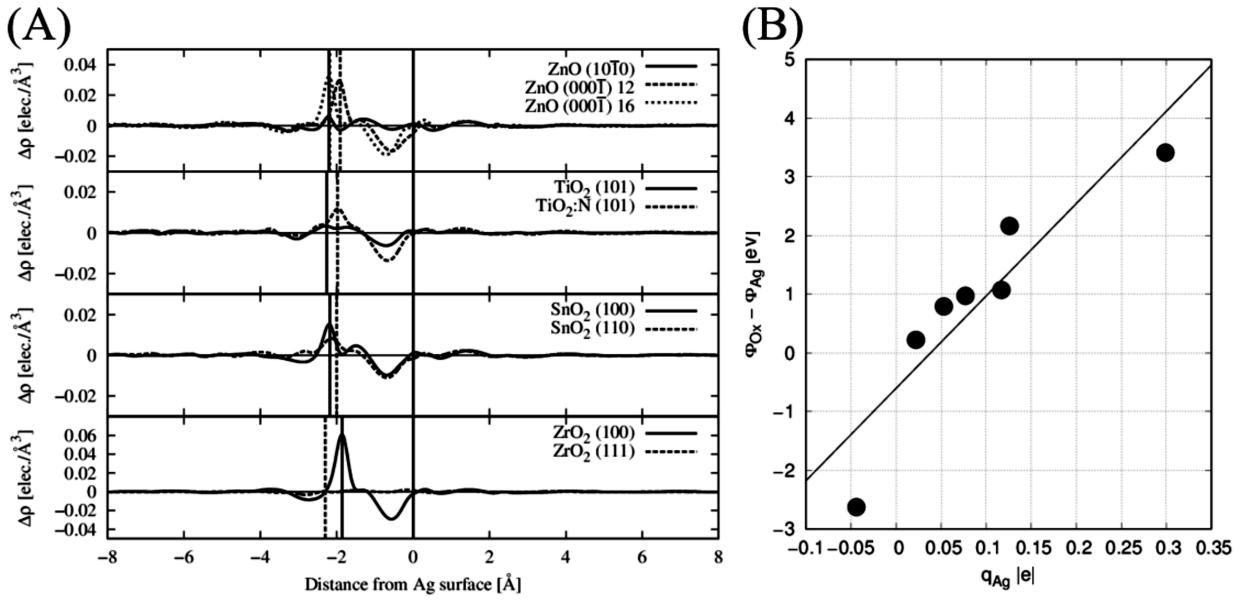

Figure 3. (A) Profile of the charge density difference for each silver/metal oxide interface. The zero reference for the distance is the average position of the silver atoms belonging to the first layer. The vertical bars at negative distances refer to the position of the metal oxide surface. (B) Correlation between the calculated charge transfer and the work function difference between the two surfaces in contact.

DOI: 10.1021/acsami.7b03269
ACS Appl. Mater. Interfaces 2017, 9, 18346−18354

metal oxide substrate. This can also be seen in Figure 3, displaying the profiles for the charge density redistribution at the various interfaces (see also B in Figure S1−9 for the corresponding 2D mapping of the charge density difference at the interface). There, a positive peak (gain in electron density) is observed in the region corresponding to the top of the oxide surface and an associated negative peak (loss in electron density) appears close to the first silver layer.

In the case of the two polar $(000\bar{1})$ ZnO surfaces 2 and 3, the same pattern intensity was observed for the electron density maps yet with a shift in the relative position of the $\Delta\rho$ peaks. The calculated average charge per silver yields a much larger charge transfer for entry 2 (0.239 |e|) compared to that for 3 (0.145 |e|), a difference that can be explained by the configuration of the silver atoms on the oxide surface. Indeed, for interface 2, each silver is adsorbed in a hollow position and bonded to three oxygen atoms, while owing to the increased packing density, only 25% of the silver atoms in contact with the oxide are sitting on hollow sites for interface 3 (see the Supporting Information, Figure S3A for a top view of the interface structure). Interface 1 involving the nonpolar $(10\bar{1}0)$ surface displays a smaller variation in the charge density pattern. The net charge transfer is difficult to visualize as the $\Delta\rho$ curve mainly presents an oscillating behavior. The corresponding q_{Ag} for this interface is only 0.022 |e|, which confirms a moderate charge donation from silver to the oxide. The difference in the charge density reorganization in the silver layers in contact with the polar versus nonpolar ZnO surfaces can be directly related to the geometry of the surface. In the case of the polar surface, the silver atoms are in close contact only with the oxygen atoms of the oxide layer. For the nonpolar surface, the surface stoichiometry is different, and the silver atoms now interact with an equivalent number of oxygen and zinc atoms. Considering the electronegativity of these three elements (O = 3.44 ; Ag = 1.93 ; Zn = 1.65), an interface involving only Ag−O interaction would promote the formation of ionic bonds and an interface charge transfer, as is the case for the polar surface. In contrast, the presence of mixed Ag−O (donation of electrons) and Ag−Zn (gain of electrons) pairs at the interface is expected to result in a much smaller effective electron transfer due to compensation effects, as indeed observed for the nonpolar surface.

The interface involving the undoped TiO_2 surface features a small amplitude in the charge density transfer with a corresponding q_{Ag} of 0.053 |e|. This value is, however, more than twice as large as that calculated for nonpolar ZnO. Very surprisingly though, the work of adhesion of silver on TiO_2 is significantly smaller than on the nonpolar ZnO (0.159 vs 0.959 J m^{-2}). This highlights the fact that the amount of charge transferred at a particular interface alone cannot be used to quantify the adhesive properties. Because the pristine (101) anatase surface of TiO_2 presents a poor adhesive character, we investigated for this surface the impact of p-type doping, induced here by substitution of oxygen by nitrogen atoms. In this case, a larger amount of charge is transferred from the silver to the doped oxide substrate (the calculated q_{Ag} reaches 0.126 |e| (see also charge density profile in Figure 4), which is accompanied by a 1 order of magnitude enhancement of W_{12}.

The two systems based on tin oxide present similar electron density maps in the region close to the top silver layer. They mostly differ in the vicinity of the oxide, a difference that is reflected in the calculated q_{Ag} with a lower value obtained for the (110) plane (0.077 |e|) compared to that of the (100) plane

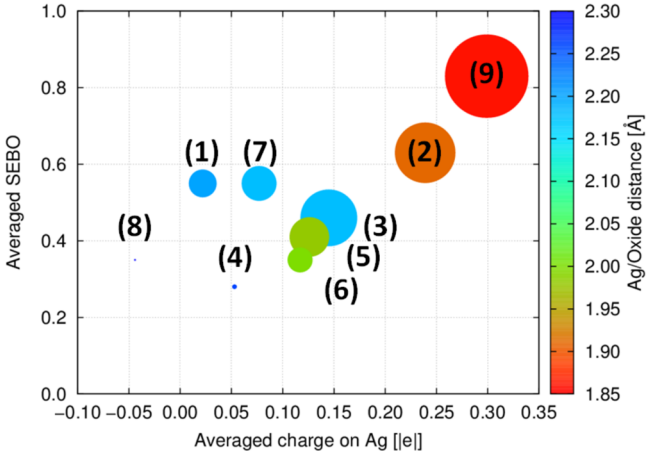

Figure 4. Four-data graph showing the amplitude of the work of separation (area of the circle) as a function of the average SEBO (*y*-axis), charge transfer (*x*-axis), and interface distance (color of the circle associated with the color code bar).

(0.117 |e|). However, these results are anticorrelated with the values of the silver work of adhesion, which is larger for the (100) plane (1.201 J m^{-2}) than for the (110) plane (0.862 J m^{-2}).

For the zirconium oxide interface, the two terminal planes yield different behaviors with a large charge transfer observed for silver adsorbed on the (100) surface and a calculated q_{Ag} of 0.299 |e|, while the charge density profile is quasi-flat for the (110) plane and even shows a charge transfer going in the opposite direction (q_{Ag} = −0.044 |e|).

It is well-known that the differences in work functions between solids drive a charge transfer at their interfaces when they are brought in contact.[66] The amount of charge transfer is governed by the work function difference between the two surfaces in contact with electron going from the lower work function material into the higher work function material to equilibrate their chemical potentials. The experimental work function of silver (111) is measured to be ca. 4.5 eV,[67] while metal oxides have work function in a range between 3.0 and 7.0 eV.[68] This is consistent with the direction of the charge transfer predicted here from ab initio calculations (with electrons flowing in most cases from the silver into the oxide). The difference in charge transfer observed between the $ZnO(10\bar{1}0)$/Ag and $ZnO(000\bar{1})$/Ag interfaces is fully consistent with the trend predicted based on their work functions (4.95 eV for $ZnO(000\bar{1})$ vs 4.64 for $ZnO(10\bar{1}0)$).[69] The small charge transfer calculated for TiO_2 is rationalized by the work function of 4.7 eV for anatase (101), i.e., close to the work function of silver.[70] The significant charge transfer calculated for the SnO_2(110)/Ag interface is in line with the higher work function reported for this oxide surface (5.4 eV).[71] An opposite charge transfer (from oxide to silver) is calculated for silver on the (111) face of ZrO_2, which is also the most stable. This is consistent with the small work function of 3.0 eV reported for this oxide.[68,72] The work function of all oxides and silver was also calculated through the computation of the electrostatic potential profile (see details in the Supporting Information). A reasonable correlation was found between the difference in work function and the amount of charge transfer among the oxides investigated (Figure 3B).

Altogether, the results reported so far show that the magnitude of the charge transfer from silver to the oxide

DOI: 10.1021/acsami.7b03269
ACS Appl. Mater. Interfaces 2017, 9, 18346−18354

does not uniquely steer the work of separation. To fully characterize the chemical interaction between silver and the metal, another descriptor has to be introduced, and we propose here the use of the effective bond order (EBO).[73] The effective bond order is the number of chemical bonds between a pair of atoms and hence provides a qualitative insight into the stability of a bond.[74] In this work, we calculated the effective bond order for each pair of atoms at the modeled interfaces. We focused our analysis on silver atoms in the first plane in contact with the oxide and calculated for these the sum of effective bond order (SEBO). SEBO is thus defined as the sum of the bond orders between a given silver atom and all atoms of the metal oxide slab (metallic or oxygen atoms, see C in Figure S1−9 in the Supporting Information for a representation of SEBO values for each interface). Finally, we used the average value of SEBO, ⟨SEBO⟩, to characterize the chemical interaction:

$$\langle \mathrm{SEBO} \rangle = \frac{1}{n} \sum_{\mathrm{Ag}} \mathrm{EBO(Ag - O)} + \mathrm{EBO(Ag - M)} \tag{5}$$

where the sum runs over the n atoms of the silver plane in contact with the metal oxide.

The calculated ⟨SEBO⟩ shows a large disparity with values ranging from 0.28 (low bonding) to 0.83 (high bonding, close to a covalent bond equal to 1). A ⟨SEBO⟩ of 0.55 is found for silver adsorbed on nonpolar ZnO (interface 1). As discussed before, this surface of ZnO is constituted by an equivalent amount of Ag−O and Ag−Zn bonds, thus leading to two populations of silver at the interface. For silver bonded to oxygen, the calculated SEBO reaches 0.59. This value is mainly dominated by the EBO of the Ag−O bond (0.40) with also a small contribution of the closest Zn atom (0.10) due to the fact that this population of silver is localized on a "top-bridge" position with bond length for Ag−O and Ag−Zn of 2.33 and 3.10 Å, respectively. The other half of the silver atoms are bonded to the oxide through a bridge position between two Zn atoms with bond length of 2.78 and 2.82 Å. The calculated SEBO is reduced to 0.52 with the main contribution coming from the two Ag−Zn bonds (EBO of 0.21 and 0.19). When moving to the polar ZnO surface (structure 2), all silver atoms are now localized on a hollow position with Ag−O lengths of 2.56, 2.63, and 2.89 Å. The SEBO increases compared to the nonpolar surface with a value of 0.63 for each silver atom. A deeper analysis of the EBO shows that this value is for a large part coming from the three Ag−O bonds, which have respective EBO of 0.22, 0.18, and 0.10. The other Ag/ZnO$(000\bar{1})$ interface 3 has by comparison a lower ⟨SEBO⟩ of only 0.46. At this interface, 25% of the silver atoms are localized on the hollow site and interact with 3 oxygen atoms with bond lengths of 2.78, 2.85, and 2.86 Å, while other silver atoms are sitting on a bridge position with bond lengths of 2.37 Å (Ag−O) and 3.08 Å (Ag−Zn). The individual SEBO analysis shows that silver atoms localized on the hollow site have SEBO of 0.40 with EBO of 0.10−0.11 for each Ag−O bond, while Ag atoms on the bridge site have a higher SEBO of 0.49, mainly originating from the Ag−O bond (0.33) with a little contribution from Ag−Zn (0.07).

The Ag/TiO_2 interface (interface 4) has the lowest calculated ⟨SEBO⟩ among all investigated systems with a value of 0.28. Due to the nature of the anatase (101) face, the calculated SEBO can fluctuate depending on the respective position of the silver with respect to the surface (see the Supporting Information, Figure S4C). The calculated SEBO for each silver atom is in a range between 0.22 and 0.27 (when facing titanium) and between 0.31 and 0.41 (when facing oxygen). The p-doped system (interface 5) shows an increase in the ⟨SEBO⟩ up to 0.41. The doping improves the SEBO in a similar way for the two populations with values between 0.30 and 0.44 when facing titanium and 0.41−0.51 when facing oxygen. This effect can be understood as follows: the substitution of oxygen by nitrogen in TiO_2 induces a depletion of electrons (p-type doping) inside the oxide. This, in turn, increases the amount of charge transfer from the silver (which acts like an electron reservoir) into the oxide, as can be seen from Table 2. As a result, the silver-oxide interface distance is reduced by more than 10%, and the associated shorter Ag−O bonds translate into a higher averaged bond order. Indeed, the average interfacial distance (calculated as the length between the silver atom in the first layer and the adjacent top oxygen atom of the titane surface) is actually reduced upon doping going from 2.26 Å for the undoped surface to 1.98 Å for the p-doped surface.

For the SnO_2/Ag interfaces, a significant difference appears between the (110) and (100) surfaces with calculated ⟨SEBO⟩ of 0.35 and 0.55, respectively. This can be correlated to the difference in the relative position of the silver atoms with respect to the oxygen atoms of the SnO_2 surface among the two planes. For the (110) surface, which has the lowest ⟨SEBO⟩, we recall that we built a model where the top of the surface is terminated by bridging oxygens (see 6 in Figure 1). Our interface model contains three bridging oxygen atoms that are bonded to the silver surface. Two of them linked one silver atom with bond lengths of 2.27 and 2.36 Å with an associated EBO (and total SEBO for the silver atom) of 0.47 (0.52) and 0.39 (0.46), respectively. The last bridging oxygen is bonded to two silver atoms with bond lengths of 2.44/2.49 Å with an associated EBO (and total SEBO for the silver atom) of 0.34 (0.40) and 0.28 (0.42). The values are comparable to the EBO (SEBO) observed for Ag−O bonds in the ZnO surfaces. However, the other silver atoms of the contact layer cannot make strong bonds with the SnO_2 surface because the next oxygen layer is localized 0.76 Å deeper compared to the bridging oxygen atoms. This leads to SEBO value for these silver atoms in a range between 0.17 and 0.34 depending on their respective position with respect to the top layer of the oxide. The (100) surface of SnO_2 has Sn and O atoms in a stoichiometric ratio. In our model, three populations of silver atoms can be considered: silvers (i) bonded to two oxygens (bridge); (ii) bonded to one oxygen (top-shifted); and (iii) bonded to tin. The silver atom bonded with two oxygen atom has a large SEBO of 0.71, mainly arising from the two O−Ag bonds (EBO of 0.38 and 0.25). The difference in EBO between the two bonds is correlated with the difference in bond lengths (2.30 versus 2.48 Å, respectively). For silver atoms only connected to one oxygen, a decrease in SEBO is observed with values in the range 0.53−0.59. The EBO of the O−Ag bond contributes for ca. 50% with values between 0.26 and 0.35, while the other significant contributions involve neighboring O and Sn atoms. Finally, the silver bonded to tin has a SEBO of 0.45 mainly originating from the O−Sn bond (EBO of 0.30).

The two Ag/ZrO_2 interfaces present a large difference in ⟨SEBO⟩ with a small value of 0.35 for the (111) ZrO_2 plane compared to 0.83 obtained with the (100) plane. The two interfaces can be seen as two limiting cases. For the (111) surface, the geometry of the top ZrO_2layer makes 50% of the oxygen atoms available to interact with the silver layer. The

DOI: 10.1021/acsami.7b03269
ACS Appl. Mater. Interfaces 2017, 9, 18346−18354

calculated SEBO values show that silver atoms interacting with those available oxygen atoms have SEBO between 0.41 and 0.46, while the other silver atoms have a smaller SEBO, in range 0.26−0.33. The picture is completely different when moving to the (100) face that exhibits a terminated oxygen layer. The high commensurability between this face and the (111) face of silver leads to an interfacial geometry where all silver atoms are localized in a bridge or bridge-hollow positions. This configuration favors strong O−Ag interactions with calculated SEBO for silver atoms between 0.68 and 0.96. A deeper analysis shows that the nature of the adsorption site of the silver (bridge versus bridge-hollow) has only a minor impact on the SEBO value, while the relative position of the first zirconium layer with respect to the silver atom has a stronger impact. Indeed, the SEBO of a silver atom on a bridge position facing no Zr atom of the first layer is calculated to be 0.91. This value decreases down to 0.78−0.81 for a similar bridge position but with the silver atom facing a zirconium atom. This behavior is more pronounced for the bridge-hollow site with SEBO decreasing from 0.96 (no Zr facing) to 0.68 (silver directly facing a zirconium).

At this stage, it is useful to merge the information provided by the charge transfer and ⟨SEBO⟩ analysis to derive structure−property relationships. From Figure 4 featuring a plot with the average charge on the silver atoms of the first layer along the *x*-axis and the average SEBO value along the *y*-axis, we group the interfaces into three populations based on the ionic (charge transfer) and covalent (⟨SEBO⟩) characters. When the charge transfer between the silver and the oxide layer is small (less than 0.10 |e| per silver) and the SEBO is inferior to 0.4, the work separation is found to be negligible. This is the case for interfaces 4 and 8. In the completely opposite regime, i.e., for simultaneously large charge transfer and high ⟨SEBO⟩, the work of adhesion dramatically increases. This is the case for interfaces 2 and 9 that reach $W_{12} \geq 2.02$ J m^{-2}. Between these two extreme limits, we observe an intermediate region where the calculated work of adhesion varies in the range between 0.8 and 1.4 J m^{-2} due to the fact that either the covalent or ionic contribution is small. Indeed, we have a small ⟨SEBO⟩ and a large charge transfer for interfaces 5 and 6 and large ⟨SEBO⟩ and small charge transfer for interfaces 1 and 7. The case of interface 3 exhibiting a much higher work of adhesion (1.96 J m^{-2}) can be explained by the higher density of silver atoms at the interface compared to the other interface models.

4. CONCLUSIONS

We characterized at the DFT level the adhesion of the silver (111) layer onto several metal oxide surfaces. For each interface, we calculated the charge transfer between the two surfaces and observed that the amplitude of the electron donating character between the metal and the metal oxide surface alone cannot be correlated to W_{12}. We then introduced an effective bond order parameter to describe the amount of covalent bonding interactions at the interfaces. With these two atomistic parameters (charge transfer and SEBO), we were able to rationalize all computed W_{12} values, which result from an interplay between charge transfer and chemical bonding effects. Such an approach can prove very useful to guide selection of interacting layers promoting good adhesive properties. From the results accumulated here, we identified several possible strategies: (1) Doping: A poor adhesive interface (such as anatase TiO_2/Ag, for example) can be tuned to provide good adhesion by doping of the metal oxide because we showed that this increases both the charge transfer and the covalent character. This improvement of the adhesive character through a design of the electronic properties of the surface opens the way to consider number of surfaces as potentially interesting for applications. (2) Surface termination: Another important aspect that needs to be addressed to promote good adhesion is the nature of the crystallographic face of the metal oxide. From the considered structures, interfaces that involve a polar metal oxide surface (i.e., ZnO(000$\bar{1}$) and ZrO_2(100)) have proven to be ideal candidates for good adhesive interfaces with silver. Because these surfaces are terminated by a full layer of oxygens, the bonding at the Ag/metal oxide interface involves Ag−O interactions that promote the adhesion. In contrary, nonpolar metal oxide surfaces imply mixed Ag−O and Ag−M interactions and lower adhesion. (3) Lattice commensurability: The interfacial geometry and silver density at the interface also play an important role. From the two Ag/ZnO(000$\bar{1}$) interfaces, we highlighted how a change in the relative position of the two contact planes affects the interfacial charge transfer and bond order. The calculations performed for SnO_2 also suggest that improved adhesive properties can be achieved using a "flat" surface such as SnO_2(100) that reduces dislocation in the silver plane compared to a surface with restructuring, e.g. SnO_2(110).

Altogether, we hope these results will be useful for the design of oxides with enhanced interfacial properties with silver in the context of low-e glass applications. As a final note, we stress that better adhesion of silver on the oxide surface is expected to yield improved electrical and optical properties of the glass at lower nominal Ag thickness, which would translate into a significant cost reduction.

■ ASSOCIATED CONTENT

Supporting Information

The following files are available free of charge. The Supporting Information is available free of charge on the ACS Publications website at DOI: 10.1021/acsami.7b03269.

(1) For each silver/oxide interface studied: (A) a top-view picture of the atomic position at the interface, (B) the 2D charge density profile, and (C) the graphical representation of calculated SEBO for each silver atom of the plane in contact with the oxide; (2) table with the calculated work function (PDF)

■ AUTHOR INFORMATION

Corresponding Author

*E-mail: David.Cornil@umons.ac.be.

ORCID

David Cornil: 0000-0002-9553-1626

Notes

The authors declare no competing financial interest.

■ ACKNOWLEDGMENTS

The research was supported by AGC Glass Europe and the Région Wallonne. Computational resources were provided by the Consortium des Équipements de Calcul Intensif (CÉCI), funded by the Fonds de la Recherche Scientifique de Belgique (F.R.S.-FNRS) under Grant 2.5020.11. J.C. and D.B. are FNRS research directors.

DOI: 10.1021/acsami.7b03269
ACS Appl. Mater. Interfaces 2017, 9, 18346−18354

REFERENCES

(1) Jelle, B. P.; Kalnaes, S. E.; Gao, T. Low-Emissivity Materials for Building Applications: A state-of-the-art Review and Future Research Perspectives. *Energy Buildings* **2015**, *96*, 329−356.

(2) Glaser, H. J. History of the Development and Industrial Production of Low Thermal Emissivity Coatings for High Heat Insulating Glass Units. *Appl. Opt.* **2008**, *47*, C193−C199.

(3) Barthel, E.; Kerjan, O.; Nael, P.; Nadaud, N. Asymmetric Silver to Oxide Adhesion in Multilayers Deposited on Glass by Sputtering. *Thin Solid Films* **2005**, *473*, 272−277.

(4) Wang, Z.; Cai, X.; Chen, Q.; Chu, P. K. Effects of Ti Transition Layer on Stability of Silver/Titanium Dioxide Multilayered Structure. *Thin Solid Films* **2007**, *515*, 3146−3150.

(5) Ando, E.; Miyazaki, M. Durability of Doped Zinc Oxide/Silver/Doped Zinc Oxide Low Emissivity Coatings in Humid Environment. *Thin Solid Films* **2008**, *516*, 4574−4577.

(6) Guillén, C.; Herrero, J. TCO/metal/TCO Structures for Energy and Flexible Electronics. *Thin Solid Films* **2011**, *520*, 1−17.

(7) Alvarez, R.; González, J. C.; Espinós, J. P.; González-Elipe, R.; Cueva, A.; Villuendas, F. Growth of Silver on ZnO and SnO_2 Thin Films Intended for Low Emissivity Applications. *Appl. Surf. Sci.* **2013**, *268*, 507−515.

(8) Yang, J.; Zhao, H.; Sha, H.; Li, J.; Zhao, L.; Chen, J.; Yu, B.; Zhang, F. Improvement of High-Temperature Resistance of the Ag-Based Multilayer Films Deposited by Magnetron Sputtering. *Mater. Lett.* **2014**, *118*, 62−65.

(9) Kulczyk-Malecka, J.; Kelly, P. J.; West, G.; Clarke, G. C. B.; Ridealgh, J. A.; Almtoft, K. P.; Greer, A. L.; Barber, Z. H. Investigation of Silver Diffusion in TiO_2/Ag/TiO_2 Coatings. *Acta Mater.* **2014**, *66*, 396−404.

(10) Yin, Y.; Lan, C.; Guo, H.; Li, C. Reactive Sputter Deposition of WO_3/Ag/WO_3 Film for Indium Tin Oxide (ITO)-Free Electrochromic Devices. *ACS Appl. Mater. Interfaces* **2016**, *8*, 3861−3867.

(11) Saiz, E.; Cannon, R. M.; Tomsia, A. P. High-Temperature Wetting and the Work of Adhesion in Metal/Oxide Systems. *Annu. Rev. Mater. Res.* **2008**, *38*, 197−226.

(12) Mattox, D. M. In *Adhesion Measurement of Thin Films, Thick Films, and Bulk Coatings*; Mittal, K., Ed.; ASTM International: West Conshohocken, PA, 1978; pp 54−62.

(13) El-Shabasy, M. Perspective of Adhesion of Thin Films. *Priod. Polytech. Elec. Eng.* **1981**, *25*, 123−134.

(14) Kinloch, A. *Adhesion and Adhesives: Science and Technology*; Springer: New York, 1987.

(15) Gaudette, F.; Suresh, S.; Evans, A.; Dehm, G.; Rühle, M. The influence of chromium addition on the toughness of γ-Niα-Al_2O_3 interfaces. *Acta Mater.* **1997**, *45*, 3503−3513.

(16) Evans, A. G.; Hutchinson, J. W.; Wei, Y. Interface Adhesion: Effects of Plasticity and Segregation. *Acta Mater.* **1999**, *47*, 4093−4113.

(17) Zhang, W.; Smith, J.; Evans, A. The connection between ab initio calculations and interface adhesion measurements on metal/oxide systems: Ni/Al_2O_3 and Cu/Al_2O_3. *Acta Mater.* **2002**, *50*, 3803−3816.

(18) Evans, A.; Mumm, D.; Hutchinson, J.; Meier, G.; Pettit, F. Mechanisms controlling the durability of thermal barrier coatings. *Prog. Mater. Sci.* **2001**, *46*, 505−553.

(19) Alfredsson, M.; Richard, C.; Catlow, A. Predicting the Metal Growth Mode and Wetting of Noble Metals Supported on c-ZrO_2. *Surf. Sci.* **2004**, *561*, 43−56.

(20) Malyi, O. I.; Kulish, V. V.; Bai, K.; Wu, P.; Chen, Z. A computational Study of the Effect of Alloying Additions on the Stability of Ni/c-ZrO_2 interfaces. *Surf. Sci.* **2013**, *611*, 5−9.

(21) Yu, M.; Trinkle, D. R. Au/TiO_2(110) Interfacial Reconstruction Stability from ab Initio. *J. Phys. Chem. C* **2011**, *115*, 17799−17805.

(22) Zhukovskii, Y. F.; Kotomin, E. A.; Jacobs, P. W. M.; Stoneham, A. M.; Harding, J. H. Modelling of Silver Adhesion on MgO(100) Surface with Defects. *J. Phys.: Condens. Matter* **2000**, *12*, 55.

(23) Dong, Y.; Brillson, L. J. First-Principles Studies of Metal(111)/ZnO{0001} Interfaces. *J. Electron. Mater.* **2008**, *37*, 743−748.

(24) Phillips, C. L.; Bristowe, P. D. First Principles Study of the Adhesion Asymmetric of a Metal/Oxide Interface. *J. Mater. Sci.* **2008**, *43*, 3960−3968.

(25) Kim, E.-G.; Brédas, J.-L. The Nature of the Aluminum/Aluminum Oxide Interface: A Nanoscale Picture of the Interfacial Structure and Energy-Level Alignment. *Org. Electron.* **2013**, *14*, 569−574.

(26) Neufeld, O.; Toroker, M. C. Novel High-Throughput Screening Approach for Functional Metal/Oxide Interfaces. *J. Chem. Theory Comput.* **2016**, *12*, 1572−1582.

(27) Doll, K.; Harrison, N. M. Theoretical Study of Chlorine Adsorption on the Ag(111) surface. *Phys. Rev. B: Condens. Matter Mater. Phys.* **2001**, *63*, 165410.

(28) Wöll, C. The Chemistry and Physics of Zinc Oxide Surfaces. *Prog. Surf. Sci.* **2007**, *82*, 55−120.

(29) Wang, Z. L. Zinc Oxide Nanostructure: Growth, Properties and Applications. *J. Phys.: Condens. Matter* **2004**, *16*, 829−858.

(30) Lin, Z.; Bristowe, P. D. Microscopic Characteristics of the Ag(111)/ZnO(0001) Interface Present in Optical Coatings. *Phys. Rev. B: Condens. Matter Mater. Phys.* **2007**, *75*, 205423.

(31) Diebold, U. The Surface Science of Titanium Dioxide. *Surf. Sci. Rep.* **2003**, *48*, 53−229.

(32) Lazzeri, M.; Vittadini, A.; Selloni, A. Structure and Energetics of Stoichiometric TiO_2 anatase surfaces. *Phys. Rev. B: Condens. Matter Mater. Phys.* **2001**, *63*, 155409.

(33) Batzill, M.; Katsiev, K.; Burst, J. M.; Diebold, U.; Chaka, A. M.; Delley, B. Gas-phase-dependent Properties of SnO_2 (110), (100), and (101) Single-crystal Surfaces: Structure, Composition, and Electronic Properties. *Phys. Rev. B: Condens. Matter Mater. Phys.* **2005**, *72*, 165414.

(34) Evarestov, R. A.; Bandura, A. V.; Proskurov, E. V. Plain DFT and Hybrid HF-DFT LCAO Calculations of SnO_2 (110) and (100) Bare and Hydroxylated Surfaces. *Phys. Status Solidi B* **2006**, *243*, 1823−1834.

(35) Postnikov, A. V.; Entel, P.; Ordejón, P. SnO_2: Bulk and Surface Simulations by an Ab Initio Numerical Local Orbitals Method. *Phase Transitions* **2002**, *75*, 143−149.

(36) Sun, C.; Du, A.; Liu, G.; Qiao, S.; Lu, G.; Smith, S. C. Formation Energies of Low-indexed Surfaces of Tin Dioxide Terminated by Nonmetals. *Solid State Commun.* **2010**, *150*, 957−960.

(37) Batzill, M.; Katsiev, K.; Diebold, U. Surface Morphologies of SnO_2(110). *Surf. Sci.* **2003**, *529*, 295−311.

(38) Xu, C.; Jiang, Y.; Yi, D.; Zhang, H.; Peng, S.; Liang, J. Interface-Level Thermodynamic Stability Diagram for in situ Internal Oxidation of Ag$(SnO_2)_p$ composites. *J. Mater. Sci.* **2015**, *50*, 1646−1654.

(39) Gennard, S.; Corà, F.; Catlow, C. R. A. Comparison of the Bulk and Surface Properties of Ceria and Zirconia by ab Initio Investigations. *J. Phys. Chem. B* **1999**, *103*, 10158−10170.

(40) Christensen, A.; Carter, E. A. First-principles Study of the Surfaces of Zirconia. *Phys. Rev. B: Condens. Matter Mater. Phys.* **1998**, *58*, 8050−8064.

(41) Luo, H.; Tian, D.; Zeng, C.; Fu, Y.; Wang, H. First-Principles Study the Behavior of Oxygen Vacancy on the Surface of ZrO_2 and $Zr_{0.97}M_{0.03}O_2$. *Comput. Condens. Matter* **2016**, DOI: 10.1016/j.cocom.2016.12.001.

(42) Guo, C.-X.; Warschkow, O.; Ellis, D. E.; Dravid, V. P.; Dickey, E. C. Oxide-Oxide Interfaces: Atomistic and Density Functional Study of Cubic-ZrO_2(100) ||NiO(111). *J. Am. Ceram. Soc.* **2001**, *84*, 2677−2684.

(43) Christensen, A.; Carter, E. A. Adhesion of Ultrathin ZrO_2(111) Films on Ni(111) from First Principles. *J. Chem. Phys.* **2001**, *114*, 5816−5831.

(44) Liu, L. M.; Wang, S. Q.; Ye, H. Q. First-Principles Study of Metal/Nitride Polar Interfaces: Ti/TiN. *Surf. Interface Anal.* **2003**, *35*, 835−841.

(45) Johnson, D. F.; Carter, E. A. Bonding and Adhesion at the SiC/Fe Interface. *J. Phys. Chem. A* **2009**, *113*, 4367−4373.

(46) Ayers, J. E. *Heteroepitaxy of Semiconductors: Theory, Growth, and Characterization*; CRC Press: Boca Raton, FL, 2007.

DOI: 10.1021/acsami.7b03269
ACS Appl. Mater. Interfaces 2017, 9, 18346−18354

(47) Martin, L.; Vallverdu, G.; Martinez, H.; le Cras, F.; Baraille, I. First Principles Calculations of Solid-Solid Interfaces: an Application to Conversion Materials for Lithium-ion Batteries. *J. Mater. Chem.* **2012**, *22*, 22063−22071.
(48) Chen, H.; Li, P.; Umezawa, N.; Abe, H.; Ye, J.; Shiraishi, K.; Ohta, A.; Miyazaki, S. Bonding and Electron Energy-Level Alignment at Metal/TiO_2 Interfaces: A Density Functional Theory Study. *J. Phys. Chem. C* **2016**, *120*, 5549−5556.
(49) Tamura, T.; Ishibashi, S.; Terakura, K.; Weng, H. First-Principles Study of the Rectifying Properties of Pt/TiO_2 interface. *Phys. Rev. B: Condens. Matter Mater. Phys.* **2009**, *80*, 195302.
(50) Zhu, L.; Hu, Q.-M.; Yang, R.; Ackland, G. J. Binding of an Oxide Layer to a Metal: The Case of Ti$\{10\bar{1}0\}$/TiO_2(100). *J. Phys. Chem. C* **2012**, *116*, 4224−4233.
(51) Wang, X.-G.; Smith, J. R. Si/Cu Interface Structure and Adhesion. *Phys. Rev. Lett.* **2005**, *95*, 156102.
(52) Grytsyuk, S.; Peskov, M. V.; Schwingenschlogl, U. First-Principles Modeling of Interfaces Between Solids with Large Lattice Mismatch: The Prototypical CoO(111)/Ni(111) Interface. *Phys. Rev. B: Condens. Matter Mater. Phys.* **2012**, *86*, 174115.
(53) Prada, S.; Rosa, M.; Giordano, L.; di Valentin, C.; Pacchioni, G. Density Functional Theory Study of TiO_2/Ag interfaces and their role in memristor devices. *Phys. Rev. B: Condens. Matter Mater. Phys.* **2011**, *83*, 245314.
(54) Farmanbar, M.; Brocks, G. First-principles Study of van der Waals Interactions and Lattice Mismatch at MoS_2/metal Interfaces. *Phys. Rev. B: Condens. Matter Mater. Phys.* **2016**, *93*, 085304.
(55) Sun, J. P.; Dai, J.; Song, Y.; Wang, Y.; Yang, R. Affinity of the Interface between Hydroxyapatite (0001) and Titanium (0001) Surfaces: A First-Principles Investigation. *ACS Appl. Mater. Interfaces* **2014**, *6*, 20738−20751.
(56) Soler, J. M.; Artacho, E.; Gale, J. D.; Garcia, A.; Junquera, J.; Ordejon, P.; Sanchez-Portal, D. The SIESTA Method for Ab Initio Order-N Materials Simulation. *J. Phys.: Condens. Matter* **2002**, *14*, 2745−2779.
(57) Perdew, J. P.; Burke, K.; Wang, Y. Generalized Gradient Approximation for the Exchange-Correlation Hole of a Many-Electron System. *Phys. Rev. B: Condens. Matter Mater. Phys.* **1996**, *54*, 16533−16539.
(58) Troullier, N.; Martins, J. L. Efficient Pseudopotentials for Plane-Wave Calculations. *Phys. Rev. B: Condens. Matter Mater. Phys.* **1991**, *43*, 1993−2005.
(59) Monkhorst, H. J.; Pack, J. D. Special Points for Brillouin-Zone Integration. *Phys. Rev. B* **1976**, *13*, 5188−5192.
(60) Limas, N. G.; Manz, T. A. Introducing DDEC6 Atomic Population Analysis: Part 2. Computed Results for a Wide Range of Periodic and Nonperiodic Materials. *RSC Adv.* **2016**, *6*, 45727−45747.
(61) Manz, T. A.; Limas, N. G. Introducing DDEC6 Atomic Population Analysis: Part 1. Charge Partitioning Theory and Methodology. *RSC Adv.* **2016**, *6*, 47771−47801.
(62) Siegel, D. J.; Hector, L. G.; Adams, J. B. Adhesion, Stability, and Bonding at Metal/Metal-carbide Interfaces: Al/WC. *Surf. Sci.* **2002**, *498*, 321−336.
(63) Kulkova, S. E.; Eremeev, S. V.; Hocker, S.; Schmauder, S. Electronic Structure and Adhesion on Metal-Aluminum-Oxide Interfaces. *Phys. Solid State* **2010**, *52*, 2589−2595.
(64) Lin, Z.; Bristowe, P. D. A Density Functional Study of the Effect of Hydrogen on the Strength of an Epitaxial Ag/ZnO Interface. *J. Appl. Phys.* **2007**, *102*, 103513.
(65) Baldereschi, A.; Baroni, S.; Resta, R. Band Offsets in Lattice-Matched Heterojunctions: A Model and First Principles Calculations for GaAs/AlAs. *Phys. Rev. Lett.* **1988**, *61*, 734−737.
(66) Leung, T. C.; Kao, C. L.; Su, W. S.; Feng, Y. J.; Chan, C. T. Relationship between surface dipole, work function and charge transfer: Some exceptions to an established rule. *Phys. Rev. B: Condens. Matter Mater. Phys.* **2003**, *68*, 195408.
(67) Chelvayohan, M.; Mee, C. H. B. Work Function Measurements on (110), (100) and (111) Surfaces of Silver. *J. Phys. C: Solid State Phys.* **1982**, *15*, 2305−2312.
(68) Greiner, M. T.; Lu, Z.-H. Thin-film metal oxides in organic semiconductor devices: their electronic structures, work functions and interfaces. *NPG Asia Mater.* **2013**, *5*, e55.
(69) Moormann, H.; Kohl, D.; Heiland, G. Work function and band bending on clean cleaved zinc oxide surfaces. *Surf. Sci.* **1979**, *80*, 261−264.
(70) Kumarasinghe, A. R.; Flavell, W. R.; Thomas, A. G.; Mallick, A. K.; Tsoutsou, D.; Chatwin, C.; Rayner, S.; Kirkham, P.; Warren, S.; Patel, S.; Christian, P.; O'Brien, P.; Grätzel, M.; Hengerer, R. Electronic properties of the interface between p-CuI and anatase-phase n-TiO_2 single crystal and nanoparticulate surfaces: A photoemission study. *J. Chem. Phys.* **2007**, *127*, 114703.
(71) Klein, A.; Körber, C.; Wachau, A.; Säuberlich, F.; Gassenbauer, Y.; Harvey, S. P.; Proffit, D. E.; Mason, T. O. Transparent Conducting Oxides for Photovoltaics: Manipulation of Fermi Level, Work Function and Energy Band Alignment. *Materials* **2010**, *3*, 4892−4914.
(72) Afanas'ev, V. V. Electron Band Alignment at Interfaces of Semiconductors with Insulating Oxides: An Internal Photoemission Study. *Adv. Condens. Matter Phys.* **2014**, *2014*, 1−30.
(73) Manz, T. A.; Sholl, D. S. *Catalysis Series*; Royal Society of Chemistry (RSC): London, 2013; pp 192−222.
(74) Bridgeman, A. J.; Cavigliasso, G.; Ireland, L. R.; Rothery, J. The Mayer Bond Order as a Tool in Inorganic Chemistry. *J. Chem. Soc. Dalton Trans., The Royal Society of Chemistry* **2001**, *14*, 2095−2108.

DOI: 10.1021/acsami.7b03269
ACS Appl. Mater. Interfaces 2017, 9, 18346−18354